Materials Advances

ROYAL SOCIETY OF CHEMISTRY

PAPER

View Article Online
View Journal | View Issue

Cite this: *Mater. Adv.*, 2026, 7, 1646

Synergistic potential of MIL-101(Cr) and reduced graphene oxide (rGO) in designing high-performance ammonia sensors

Shrinivas C. Motekar,[ab] Govind G. Umarji,[b] Amol G. Kadlag,[bc] Bharat B. Kale [b] and Sudhir S. Arbuj *[b]

The confluence of metal–organic frameworks (MOFs) and conductive materials has revolutionized gas sensing technology. This study presents a synergistic composite of MIL-101(Cr) and reduced graphene oxide (rGO) for enhanced ammonia gas sensing. rGO–MIL-101(Cr) composites with varying weight percentages of MIL-101(Cr) were synthesized and further characterised using various techniques. By harnessing the exceptional surface area and tailored pore structure of MIL-101(Cr) in tandem with the superior conductivity of rGO, the composite exhibits remarkable sensitivity and fast response times. Among the prepared compositions, rGO–20 wt% MIL-101 (Cr) has demonstrated exceptional sensitivity towards ammonia detection, with a sensitivity of −18.87 for 60 000 ppm and −5.24% for 2000 ppm of ammonia gas and a discernible response at concentrations as low as 1 ppm. Notably, the composite's response remained remarkably consistent and stable, even after one year. This outstanding durability and stability underscore the composite's potential for reliable and long-term ammonia sensing applications. At this percentage, the highest sensitivity is due to the perfect coordination bonding between ammonia molecules and the chromium nodes in MIL-101(Cr), modulating its electrical properties. The formation of a perfect interface between MIL-101 (Cr) and rGO facilitates efficient charge transport, thereby enabling precise detection of ammonia gas. The FE-SEM and TEM analyses clearly show the presence of such an interface. Notwithstanding the comparable or superior sensing capabilities of existing ammonia sensors under optimal conditions, their practical utility is frequently compromised by the susceptibility of the constituent materials to humidity. In contrast, our rGO–MIL-101(Cr) composite exhibits a unique synergy of outstanding sensing performance and notable stability under moist conditions due to its remarkably high surface area and durable architecture. This exclusive combination of properties enables our material to surpass the performance of existing sensors in real-world settings, where moisture is a common factor, and thus offers a significant advantage over existing sensors. This research highlights the potential of MOF-based composites for advanced gas sensing applications, paving the way for further exploration and development of novel sensing platforms.

Received 26th September 2025,
Accepted 16th December 2025

DOI: 10.1039/d5ma01104c

rsc.li/materials-advances

1 Introduction

Since 2003, following the pioneering work of Yaghi and co-workers on porous and high-surface-area metal–organic frameworks (MOFs), these materials have garnered significant attention for their potential in gas storage and detection. MOFs are an extensive class of highly crystalline inorganic–organic hybrids assembled from metal clusters (secondary building units) linked by multidentate organic ligands, creating a three-dimensional network of micropores (typically <2 nm) and channels. The organic ligands used are primarily carboxylates and/or nitrogen-containing heterocycles, while metal ions such as zinc, copper, and first-row transition metals are commonly employed. MOFs are characterized by their robust structures, high specific surface areas, and permanent porosity. The rigidity of organic carboxylate linkers contributes to the exceptional robustness of the porous framework, which is maintained even after solvent evacuation. As highlighted in the review by O'Keeffe and Yaghi, the combination of metal ion clusters and organic ligands yields numerous possible network

[a] *Department of Chemistry, Sunderrao Solanke Mahavidyalaya, Majalgaon, Beed-431131, Maharashtra, India. E-mail: shrimotekar@gmail.com*
[b] *Centre for Materials for Electronics Technology, Affiliated to Savitribai Phule Pune University, Off Pashan Road, Panchawati, Pune-411008, Maharashtra, India. E-mail: sudhir1305@gmail.com, sudhir@cmet.gov.in*
[c] *Department of Chemistry & Research Centre, S. N. Arts, D.J.Malpani Commerce & B.N.Sarda, Science college, (Autonomous), Affiliated to Savitribai Phule Pune University, Sangamner, 422605, Pune, Maharashtra, India*

topologies. MOFs have shown considerable potential in gas detection, leveraging their ultrahigh surface areas, tunable pore sizes, and predictable framework topologies. The reticular synthesis approach enables pore size enhancement and functionalization of pore walls, making MOFs highly versatile.[1,2] Despite these advantages, practical applications of MOFs still face several challenges.

The significance of ammonia (NH_3) in diverse industrial sectors, including agriculture and chemical manufacturing, is underscored by its pivotal role in the production of essential commodities such as fertilizers, synthetic fibers, plastics, and pharmaceuticals. However, the liberation of NH_3 during industrial processes and natural events poses substantial health risks owing to its toxicological profile. Acute exposure to elevated NH_3 concentrations can precipitate severe ocular and respiratory irritation, whereas protracted exposure to lower concentrations can culminate in lasting pulmonary damage, thereby emphasizing the imperative need for stringent monitoring and control measures.[3] The Occupational Safety and Health Administration (OSHA) has promulgated permissible exposure limits (PELs) for NH_3, specifying threshold values of 25 ppm over an 8-hour time-weighted average and 35 ppm for 15-minute short-term exposure intervals.[3] Consequently, the development of advanced sensing materials capable of selectively detecting NH_3 in complex gas mixtures, replete with volatile organic compounds (VOCs) and other interfering gases, assumes paramount importance.

Although various NH_3 sensing techniques have been explored,[3–16] including metal oxide-based sensors, conducting polymers, optical sensors, MOF based sensors, one-dimensional photonic crystal sensors and electrochemical sensors, this investigation focuses on the chromium-based MOF MIL-101(Cr) owing to its exceptional porosity, high surface area, and remarkable chemical stability. Notably, MIL-101(Cr) has demonstrated efficacy in capturing NH_3,[17] thereby underscoring its potential as a sensing material. By integrating MIL-101(Cr) with reduced graphene oxide (rGO), we aim to synergistically enhance the detection capabilities for ammonia gas, leveraging the unique properties of both materials to create a high-performance sensing platform. The chromium-based metal–organic framework MIL-101(Cr) possesses a unique hierarchical structure, wherein trimeric Cr(III) octahedral clusters are linked by benzene-1,4-dicarboxylate (BDC) ligands to form a zeotype architecture. This framework features two distinct mesoporous cages, approximately 2.9 nm and 3.4 nm in diameter, which are accessible through windows of corresponding sizes.

MIL-101(Cr)'s exceptional adsorption capacity, high surface area, and tailored pore structure render it an attractive material for sensing applications. Despite its inherent limitations in electrical conductivity, MIL-101(Cr) has been successfully employed as a sensing layer in various transduction platforms, including quartz crystal microbalances and interdigitated electrode transducers.[18,19] Notably, MIL-101(Cr) exhibits remarkable hydrothermal stability, maintaining its structural integrity and porosity even under prolonged exposure to boiling water.[20] This stability, combined with its high sensitivity and selectivity, positions MIL-101(Cr) as a promising candidate for gas sensing applications in complex environments. The integration of MIL-101(Cr) with rGO may potentially enhance its electrical properties, thereby enabling the development of advanced sensing platforms with improved performance.

Graphene, renowned for its exceptional electronic conductivity, has emerged as a leading material in the carbon family, garnering extensive utilization in gas sensing applications. Its derivatives, rGO and graphene oxide (GO), have also garnered significant attention for synthesizing functional materials. Notably, rGO exhibits superior conductivity compared to GO, rendering it an attractive candidate for sensing applications.[21] While GO has been employed in conjunction with MIL-101(Cr) for ammonia gas sensing,[3] the substitution of GO with rGO is anticipated to yield enhanced results due to its higher conductivity. The unexplored potential of rGO–MIL-101(Cr) composites in ammonia gas sensing presents a promising avenue for investigation. The integration of rGO with MIL-101(Cr) is a judicious choice, as it significantly enhances the composite's conductivity, thereby accelerating electron transfer and facilitating improved sensing performance.

Consequently, the rGO–MIL-101(Cr) composite is expected to exhibit exceptional sensitivity towards ammonia gas, underscoring the potential of combining these materials to achieve high-performance composites. While existing ammonia sensors may exhibit comparable or even superior sensing performance under ideal conditions, they often employ materials that are unstable in humid environments, limiting their practical applications. In contrast, our rGO–MIL-101(Cr) composite combines excellent sensing performance with remarkable water stability, attributed to the ultra-high specific surface area and robust framework of MIL-101(Cr). This unique combination enables our material to outperform existing sensors under real-world conditions, where moisture is often present. Notably, the composite's response remained remarkably consistent and stable, even after one year. This synergy between rGO and MIL-101(Cr) may ultimately yield advanced sensing platforms with improved efficacy.

2. Experimental section

2.1. Chemicals

Chromic nitrate nonahydrate ($Cr(NO_3)_3$ $9H_2O$), terephthalic acid (H_2BDC), *N*,*N*-dimethylformamide (DMF), reduced graphene oxide (rGO), and ethanol (CH_3CH_2OH) were purchased from Sigma-Aldrich. All chemicals were of analytical grade with 99% purity and used as received without further purification. All the solutions were prepared in deionized water.

2.2. Synthesis of MIL-101(Cr)

MIL-101(Cr) synthesis was optimized using the following variations (Table 1) to obtain the best surface area. The synthesis procedure for the optimized MIL-101(Cr) is given below.

Initially, 4.0021 g (10 mmol) of chromium nitrate nonahydrate was dissolved in 30 mL distilled water under continuous

Table 1 Synthesis parameters for MIL-101(Cr) optimization and rGO–MIL-101(Cr) composites

S. No.	Codes	HF amount (mL)	Mole ratio of chromium nitrate : terephthalic acid	Temperature (°C)	Time (h)
1	a	0.4	1 : 1	220	8
2	b	0.6	1 : 1	220	8
3	c	0.8	1 : 1	220	8
4	d	1.0	1 : 1	220	8
5	e	0.4	1 : 1.5	220	8
6	f	0.4	1 : 2	220	8
7	g	0.4	1 : 1	180	8
8	h	0.4	1 : 1	200	8
9	No product	0.4	1 : 1	220	4
10	i	0.4	1 : 1	220	12

	Codes	rGO–MIL-101(Cr) composites with different wt% of MIL-101(Cr)
11	j	0 (pristine rGO)
12	k	2.5
13	l	5
14	m	10
15	n	15
16	o	20
17	p	40
18	q	60
19	r	80

magnetic stirring. Meanwhile, 1.6613 g (10 mmol) of terephthalic acid was separately stirred in 30 mL of distilled water. After 30 min, two solutions were mixed and stirred for 30 min. Furthermore, 0.4 mL of HF was added dropwise to this mixture and the mixture was again stirred gently for 30 min. This mixture was transferred into a 100 mL Teflon lined stainless steel autoclave and then sealed. The autoclave was maintained at 220 °C for 8 h and then cooled naturally to room temperature. The as-synthesized greenish product was centrifuged. This product was then dispersed in 100 mL distilled water and again stirred for 30 min at 90 °C, cooled naturally, centrifuged, filtered and rinsed with hot distilled water several times until the greenish colour of the supernatant liquid vanished. After this, the same process was repeated several times with 100 mL DMF under stirring for 1 h at 120 °C, cooled naturally, centrifuged and filtered to ensure the complete removal of white crystals of unreacted terephthalic acid. The product was dispersed in 100 mL ethanol, stirred for 30 min at 60 °C, cooled naturally, centrifuged, and filtered. This process was repeated three to five times to ensure the complete removal of guest DMF molecules. Then the separated solid was dried at 80 °C in a vacuum oven for 12 h, allowed to cool to room temperature naturally, and ground well to obtain the MIL-101 crystals with uniform size.

2.3. Synthesis of rGO/MIL-101(Cr) composites

A series of rGO–MIL-101(Cr) composites were prepared with varying the weight percentage of MIL-101(Cr) as 2.5, 5, 10, 15, 20, 40, 60 and 80. rGO and MIL-101(Cr) were mixed well and ground in a mortar and pestle for 30 min to obtain a uniform mixture. The formed composites were used for further characterization and gas sensing applications.

2.4. Characterization of MIL-101(Cr)

The prepared rGO, optimized MIL-101(Cr) and rGO–MIL-101(Cr) composites were analyzed by powder X-ray diffraction (XRD) using a Rigaku MiniFlex equipped with a monochromator and a Ni-filtered Cu Kα radiation source (wavelength = 1.5418 Å) in the 2θ range of 1°–80°. Fourier transform infrared (FTIR) spectra were recorded using a Shimadzu IRAffinity-1S WL model equipped with a Quest diamond attenuated total reflection (ATR) accessory in the range of 475–4000 cm^{-1}. The morphology of the as-synthesized samples was observed by field emission scanning electron microscopy (FESEM, HITACHI S4800, ZEISS GeminiSEM 560). The high-resolution transmission electron microscopy (HRTEM) images and selected area electron diffraction (SAED) patterns were also recorded using a JEOL JEM-200FS. The chemical compositions were determined by X-ray photoelectron spectroscopy (XPS); for XPS measurements, a Thermo Scientific NEXSA equipped with an Al Kα X-ray source (1486.6 eV) was used. The surface area, pore size, and pore volume of rGO and the prepared MIL-101(Cr) and rGO–MIL-101(Cr) composite nanostructures were calculated from the N_2 adsorption–desorption isotherms recorded at liquid nitrogen temperature using a Quantachrome NOVA Touch LX[1] instrument. The samples were degassed in a vacuum at 100 °C for 1 h prior to surface area analysis.

2.5. Gas sensing measurement

The gas sensing apparatus is a custom-designed setup comprising a 500 mL glass chamber, a KEYSIGHT DAQ970A Data Acquisition System for data logging, and a printed circuit board (PCB) with an interdigitated (ITD) pattern of 4 fingers and a 3 mm diameter active area where the sensing material (rGO–MIL-101(Cr) composite) is deposited and interacts with the target gas (ammonia). 10 mg of the composite material was dispersed in 1 mL of ethanol and sonicated for 5 minutes. A drop of the dispersed solution was placed on the 3 mm active area of the ITD pattern PCB and dried in a vacuum oven at 100 °C for 2 h. The PCB is designed in a such way that nine samples can be tested in one slot. In this experiment, a particular volume of ammonia gas ranging from 30 mL to 1 mL (6% to 0.2%, *i.e.* 60 000 ppm to 2000 ppm) was injected into the 500 mL glass chamber using a syringe and further down to 1 ppm using a dilution technique. This static system utilizes the glass chamber as a controlled environment for gas introduction and measurement, allowing precise control over experimental conditions. The data logging system features a high-resolution display and multiple input channels, enabling simultaneous measurement and recording of temperature and resistance. The PCB, with the deposited rGO–MIL-101(Cr) composite, acts as the sensing platform, facilitating the detection of ammonia gas through changes in electrical resistance. The same reaction setup was utilized for measuring the cross sensitivity for gases such as acetone, chloroform, toluene, benzene, methanol and hydrogen. These gases were injected in a volume of 25 mL only (5%, *i.e.* 50 000 ppm).

3. Results and discussion

3.1. X-ray diffraction analysis

The XRD pattern of the synthesized MIL-101(Cr) material with varying amounts of HF, mole ratio of reactants, reaction temperature and time, depicted in Fig. S1 (SI), shows diffraction peaks that are indexed to specific crystal planes and match well with the characteristic XRD pattern of MIL-101, validating the formation of this MOF.[22] No additional diffraction peaks were detected, suggesting the absence of crystalline impurities or secondary phases.[23] This observation confirms the phase purity of the sample, which exhibits a well-defined crystalline structure. Furthermore, the presence of intense peaks at low angles is indicative of the material's high porosity.[24]

The XRD pattern of pristine rGO reveals a distinct peak at 26.4° (2θ), corresponding to an interplanar spacing of 3.6 Å (shown in Fig. 1). This peak is attributed to the (002) crystallographic plane, indicative of rGO's layered architecture.[25] This peak is a hallmark of the hexagonal graphene structure, providing evidence for the effective reduction of graphene oxide to rGO. The presence of a peak at 43.28° (2θ) is associated with the turbostratic structure of disordered carbon.[26] The absence of a diffraction peak in the 2θ range of 10–12° in rGO is indicative of effective reduction, signifying substantial elimination of oxygenated functional groups inherent to graphene oxide.[27] The XRD pattern of rGO nanoparticles is consistent with JCPDS card no. 89-7213, confirming the material's crystalline structure.[28] The as-prepared rGO–MIL-101(Cr) composite retains the primary patterns of both the pristine MOF and rGO, indicating the successful formation of the composite material. As the wt% of MIL-101(Cr) increases, the corresponding peak intensities at 2.8°, 5.16°, 8.42° and 9.03° increase [from k to r (see Table 1)] and starts to appear from 5 wt% onwards (Fig. 1), whereas with the decrease of the wt% of rGO, the corresponding peak intensities at 26.4° and 43.28° start to diminish [from j to r (see Table 1)], indicating the formation of a composite between rGO and MIL-01(Cr).

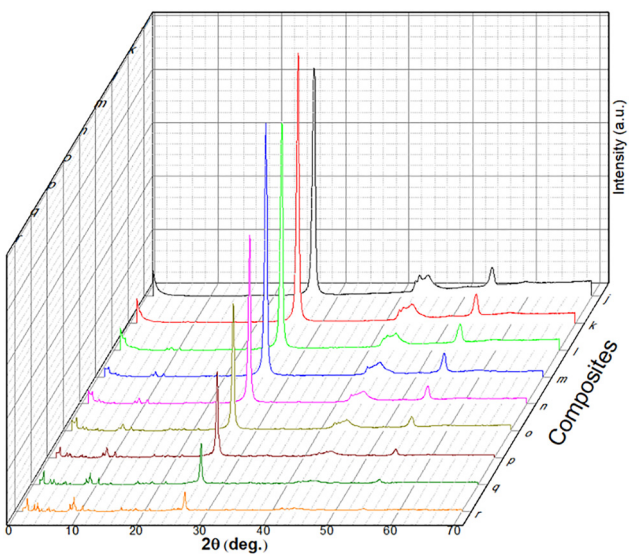

Fig. 1 XRD patterns of rGO and rGO–MIL-101(Cr) composites with varying MIL-101(Cr).

3.2. FTIR spectroscopy analysis

The FTIR spectrum of our optimized MIL-101(Cr) sample (Fig. 2) exhibits three prominent absorption peaks at 1394 cm^{-1}, 1510 cm^{-1}, and 1629 cm^{-1}, which are attributed to the symmetric stretching vibration of O–C–O, the asymmetric stretching vibration of C═O in dicarboxylate, and the C═C stretching vibration in the aromatic ring, respectively. These characteristic peaks confirm successful incorporation of the linker into the MIL-101(Cr) framework. The deformation vibrations of C–H are observed at 1160 cm^{-1}, 1017 cm^{-1}, 880 cm^{-1}, and 746 cm^{-1}, while the Cr–O vibration band at 580 cm^{-1} provides evidence for the formation of MIL-101(Cr), indicating that the material has been synthesized as intended.[29,30] The FTIR spectrum shows no evidence of adsorbed water in the MIL-101(Cr) pores, as indicated by the absence of a peak at 1640 cm^{-1}, even after exposure to air.[31] Unreacted terephthalic acid trapped inside and outside the pores of MIL-101(Cr) can lead to a reduction in surface area and pore volume. The absence of the peak at 1669 cm^{-1} indicates that no unreacted H_2BDC is present in the pores.[30]

3.3. BET surface area analysis

Our objective was to synthesize MIL-101(Cr) with optimal surface area, and to achieve this, we optimized the reaction conditions. Initially, we investigated the effect of varying the hydrofluoric acid (HF) amount (0.4 mL, 0.6 mL, 0.8 mL, and 1 mL) on the synthesis of MIL-101(Cr) with a 1 : 1 mole ratio of chromium nitrate and terephthalic acid. The reactions were carried out in an autoclave at 220 °C for 8 h. As previously reported by Loiseau and Ferey, fluorine acts as a mineralizing agent that enhances the crystallinity of microporous materials and promotes the formation of highly crystalline phases in MOFs.[32] We observed that a pH below 2 resulted in high crystallinity of MIL-101(Cr), and 0.4 mL of HF was sufficient to achieve this. Notably, we obtained a 57% yield with a BET

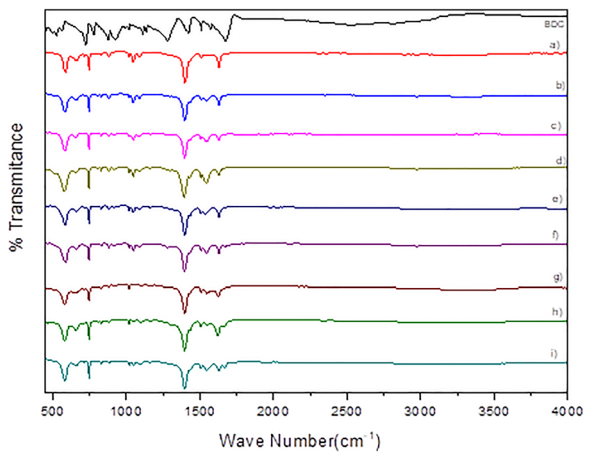

Fig. 2 FTIR spectra of MIL-101(Cr) with different variations (a) to (i) and BDC.

surface area of 2717.5 m^2 g^{-1} when using 0.4 mL of HF. In contrast, higher HF concentrations (0.6 mL, 0.8 mL, and 1 mL) resulted in lower yields (28%, 26%, and 24%, respectively) and decreased surface areas (2046.4 m^2 g^{-1}, 1285.4 m^2 g^{-1}, and 1117.9 m^2 g^{-1}, respectively). The higher HF concentrations also led to increased amounts of unreacted terephthalic acid, which required additional washing with DMF and reduced the product yield. Furthermore, repeated washing with distilled water was necessary to remove the greenish color of the supernatant liquid, which was attributed to unreacted chromium nitrate. If DMF molecules are not completely removed, they remain occluded in the two types of mesoporous cages of MIL-101(Cr). To ensure complete removal of guest DMF molecules, we performed repeated washing with ethanol by stirring for 30 min at 60 °C. Our results indicate that 0.4 mL of HF maintains the optimal pH for maximum reaction completion, resulting in the highest product yield and porosity and consequently the maximum surface area.

Next, we investigated the effect of varying the mole ratio of terephthalic acid (1, 1.5, and 2 moles) while keeping the HF amount constant at 0.4 mL. The reactions were carried out at 220 °C for 8 h. We observed that increasing the amount of terephthalic acid resulted in higher amounts of unreacted terephthalic acid, which required additional washing with DMF and reduced the product yield. Moreover, the increased terephthalic acid concentration negatively affected the porosity of the product, as evident from the decreased surface areas (2294.2 m^2 g^{-1} and 1702.1 m^2 g^{-1} for 1.5 and 2 moles, respectively). These results confirm that the optimal conditions for synthesizing MIL-101(Cr) with the highest surface area and maximum reaction completion are 0.4 mL of HF and a 1 : 1 mole ratio of chromium nitrate and terephthalic acid.

Subsequently, we investigated the effect of reaction temperature (180, 200, and 220 °C) on the synthesis of MIL-101(Cr) while keeping the other parameters constant. At 180 °C, the product exhibited a lower surface area (2351.3 m^2 g^{-1}) and a notably lower yield (1.32%). This suggests that only a few reactant molecules had sufficient energy to overcome the activation energy barrier and contribute to product formation, resulting in reduced porosity. When the temperature was increased to 200 °C, the product yield significantly increased to 27.34%, accompanied by a BET surface area of 2705.1 m^2 g^{-1}. This indicates that a greater number of molecules participated in product formation, and the crystallinity of the MIL-101 phase was slightly enhanced. Temperature plays a crucial role in the hydrothermal synthesis of MIL-101, influencing the condensation of chromium clusters and material crystallization. The controlled temperature and pressure environment of the solvothermal technique facilitates effective reactant interactions, thereby enhancing the product yield. Furthermore, the coordination of metallic species, nuclearity, and dimensionality of the inorganic subnetwork in MOFs are known to be strongly dependent on the reaction temperature.[33–35] Based on our results, 220 °C appears to be the optimal temperature for the synthesis of MIL-101(Cr), yielding the best results in terms of surface area and product yield.

Finally, we investigated the effect of reaction time (4, 8, and 12 h) on the synthesis of MIL-101(Cr) while keeping the other parameters constant. No product formation was observed for the 4 h reaction time. The 12 h reaction time resulted in a lower product yield (42.66%) and surface area (1810.9 m^2 g^{-1}) compared to the 8 h reaction time. The XRD peaks for the 8 h reaction time were sharper and more intense than those for the 12 h product. Our results indicate that the optimal conditions for synthesizing MIL-101(Cr) with the highest surface area and crystallinity are 0.4 mL of HF, an equimolar ratio of reactants, a reaction temperature of 220 °C, and a reaction time of 8 h.

The nitrogen adsorption–desorption isotherms for rGO, MIL-101(Cr), and their composites are shown in Fig. 3. The isotherm exhibits a type IV characteristic with a pronounced hysteresis loop, indicative of the mesoporous nature of MIL-101(Cr) at loadings exceeding 10%. In contrast, lower MIL-101(Cr) loadings result in a type III isotherm, suggesting weak interactions between the adsorbate and adsorbent molecules. Notably, further increases in MIL-101 loading beyond 15% do not yield a discernible hysteresis loop, implying the absence of larger pore structures within the sample. A systematic increase in MIL-101 loading leads to a corresponding enhancement in surface area, ranging from 57.6 m^2 g^{-1} (2.5 wt%) to 1269.6 m^2 g^{-1} (80 wt%). The surface area, average pore radius, and pore volume are summarized in Table 2. The adsorption isotherm exhibits two distinct steps at a relative pressure (P/P_0) of 0.2, which can be attributed to the bimodal distribution of mesoporous channels in MIL-101(Cr), a characteristic feature of its nitrogen adsorption–desorption isotherm.

Fig. 4 presents the Barrett–Joyner–Halenda (BJH) curve, which illustrates the pore size distribution of the samples. The pore sizes are found to range from approximately 3.5 to 25 nm, confirming the mesoporous nature of the materials. Notably, as the MIL-101(Cr) loading increases, the average pore radius decreases, while the total pore volume exhibits a corresponding increase. The detailed values of these parameters are summarized in Table 2.

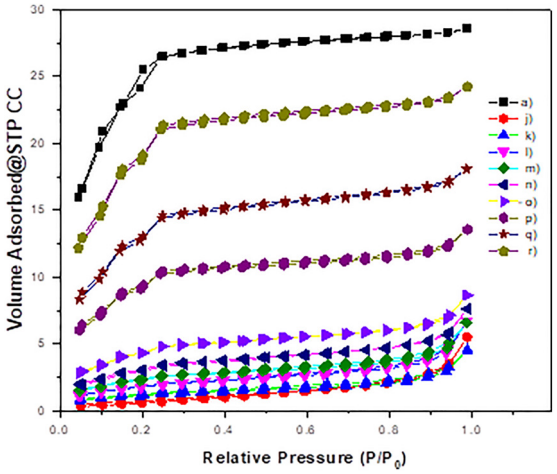

Fig. 3 N_2 adsorption–desorption isotherms of rGO, MIL-101(Cr) and their composites.

Table 2 The surface area, average pore radius and total pore volume of rGO, MIL-101(Cr) and their composites

S. No.	Sample codes	Samples	BET surface area (m^2 g^{-1})	Average pore radius (nm)	Total pore volume (cc g^{-1})
1	a	MIL-101(Cr)	2717.5	1.0223	1.389
2	j	rGO	37.5	5.7393	0.09165
3	k	2.5%	57.8	3.3007	0.09549
4	l	5%	90.2	3.0643	0.13523
5	m	10%	114.2	2.3688	0.13824
6	n	15%	193.6	2.0152	0.1951
7	o	20%	258.4	1.6523	0.21351
8	p	40%	470.0	1.2214	0.28704
9	q	60%	888.8	1.1601	0.51555
10	r	80%	1269.7	1.0726	0.68092

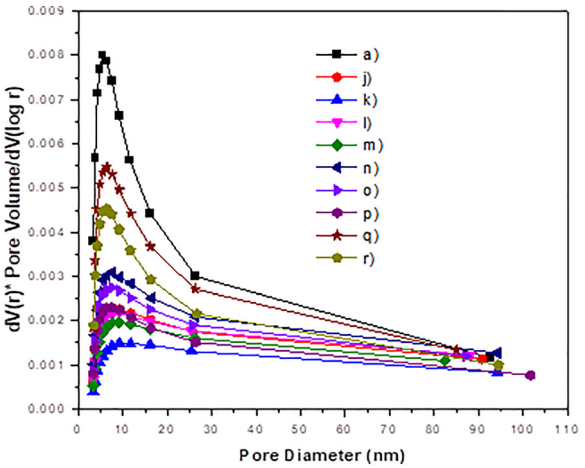

Fig. 4 The BJH pore size distribution curves of rGO, MIL-101(Cr) and their composites.

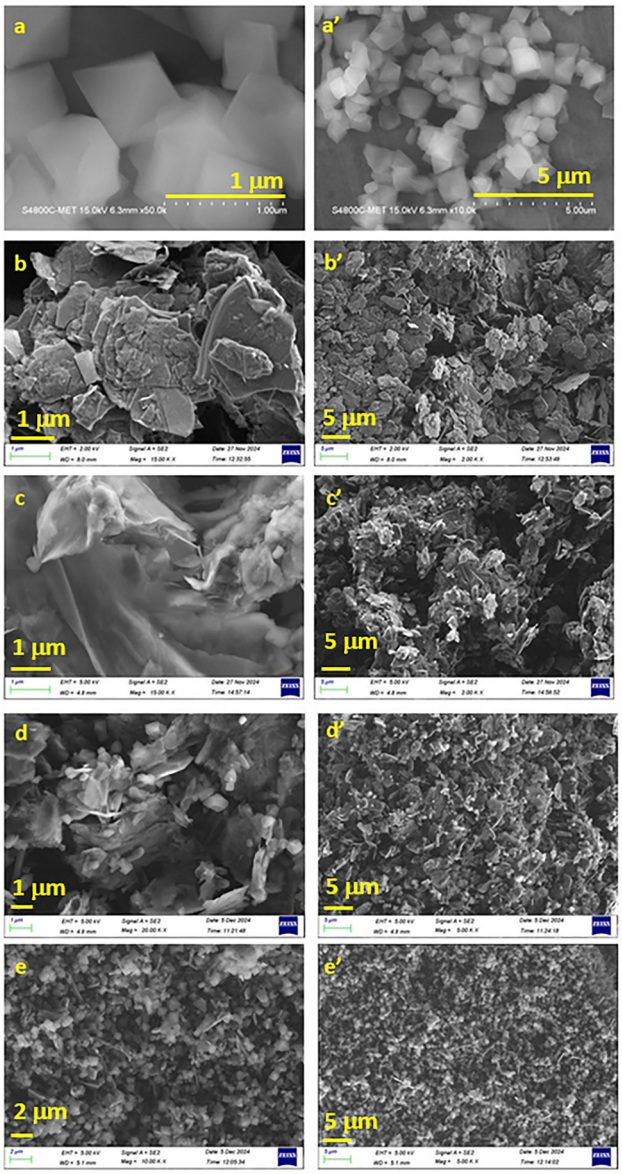

Fig. 5 FESEM images of (a) and (a′) pristine MIL-101(Cr), (b) and (b′) pure rGO, (c) and (c′) 2.5% MIL-101(Cr) composite, (d) and (d′) 20% MIL-101(Cr) composite, and (e) and (e′) 80% MIL-101(Cr) composite.

3.4. Morphological and nanostructural analyses

3.4.1. FESEM analysis of the synthesised MIL-101(Cr) samples and rGO–MIL-101(Cr) composites. The morphological characteristics of the composite and pure components were examined using FESEM, as illustrated in Fig. 5. The SEM micrographs of MIL-101(Cr) (Fig. 5a and a′) reveal a regular octahedral morphology[36] with a smooth surface and an average size of approximately 400 nm. The rGO nanosheets (Fig. 5b and b′) exhibit corrugations due to the aggregation of graphene layers,[37] with lateral dimensions ranging from 0.5 to 3 µm.

The FESEM images of the composites demonstrate a uniform distribution of MIL-101(Cr) crystals over the rGO sheets. Specifically, the 2.5 wt% MIL-101(Cr) composite (Fig. 5c and c′) shows a sparse yet uniform dispersion of MIL-101(Cr) crystals. As the MIL-101(Cr) content increases to 20 wt% (Fig. 5d and d′), the crystal density on the rGO surface increases while maintaining uniform distribution. At higher MIL-101(Cr) loadings (80 wt%, Fig. 5e and e′), the MIL-101(Cr) crystals densely cover the entire surface of the rGO sheets.

3.4.2. FETEM analysis of the synthesised MIL-101(Cr) samples and rGO–MIL-101(Cr) composites. The microstructural characteristics of pristine MIL-101(Cr), rGO, and the 20 wt% MIL-101(Cr) composite were examined using FETEM, as depicted in Fig. 6. The pristine MIL-101(Cr) crystals exhibit a regular octahedral morphology with sharp edges, measuring 500–600 nm in size (Fig. 6a and b). The corresponding SAED pattern reveals a diffuse ring, indicative of the polycrystalline

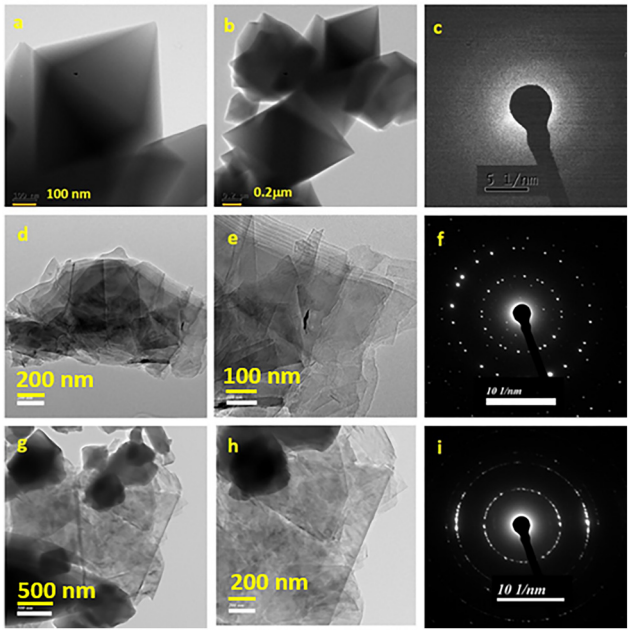

Fig. 6 TEM images and SAED patterns of (a)–(c) pristine MIL-101(Cr), (d)–(f) pure rGO, and (g)–(i) 20% MIL-101(Cr) composite.

nature of MIL-101(Cr), which is consistent with the PXRD results. The composites demonstrate a uniform distribution of MIL-101(Cr) crystals within a 3D interconnected network on the rGO sheets. This uniform mixing of rGO and MIL-101(Cr) is evident, with a large number of MIL-101(Cr) crystals adhering to the rGO surface, confirming the successful synthesis of the composite. The rGO nanosheets exhibit corrugations due to the aggregation of graphene layers, with lateral dimensions ranging from 0.5 to 3 μm (Fig. 6d and e). The TEM images reveal that the rGO sample comprises nanosheets with a smooth surface, consistent with the SEM observations (Fig. 5b and b′). Furthermore, the separate layers of rGO are distinctly visible in Fig. 5e, where the transparent regions indicate single graphene layer structures, and the dark regions signify overlapping of layers. The SAED pattern of the rGO sheets (Fig. 6f) displays bright spots, indicating their highly crystalline nature. In the composite, the presence of MIL-101(Cr) octahedrons on the rGO surface is clearly evident (Fig. 6g and h). The SAED pattern further confirms the presence of highly crystalline MIL-101(Cr) in the composite, as indicated by the bright spots.

3.5. XPS analysis

The surface properties of rGO and the 20% MIL-101(Cr) composite were investigated using XPS analysis, as presented in Fig. 7 and 8, respectively. The XPS survey spectra of rGO (Fig. 7a) reveal the presence of two primary elements: carbon (C 1s) and oxygen (O 1s), centered at binding energies of 284.5 eV and 532.2 eV, respectively. The high-resolution C 1s spectrum of rGO (Fig. 7b) recorded a dominant peak at 284.5 eV, attributed to graphitic carbon. Additionally, shoulder peaks are observed at 285.3 eV, 287 eV, and 291.3 eV, corresponding to C–OH, C═O, and O–C═O, respectively. The O 1s spectrum of rGO

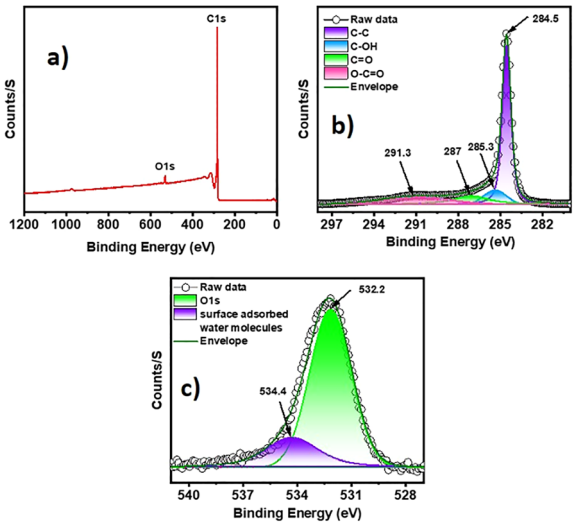

Fig. 7 XPS analysis of rGO: (a) wide scan spectra and high resolution (b) C 1s and (c) O 1s spectra.

(Fig. 7c) shows a primary peak at 532.2 eV, assigned to oxygen in rGO.[38] A smaller peak at 534.4 eV is attributed to surface-adsorbed water molecules.

The XPS spectrum of the 20% MIL-101(Cr) composite (Fig. 8a) showed similar peaks to those observed in the XPS spectrum of rGO, with the additional presence of Cr peaks. The high-resolution C 1s spectrum (Fig. 8b) shows a peak at 284.5 eV, attributed to the C–C bond in rGO. Furthermore, peaks at 285.6 eV, 287.8 eV, and 290.8 eV correspond to carbon atoms in the BDC linker and rGO, specifically C–C, C═O, and O–C═O, respectively. The slight shifts in the carbon peaks confirm the formation of the MIL-101(Cr) and rGO composite. The high-resolution Cr 2p spectrum (Fig. 8c) displays two major peaks at 577.5 eV (Cr $2p_{3/2}$) and 587.2 eV (Cr $2p_{1/2}$), assigned to Cr^{3+}.

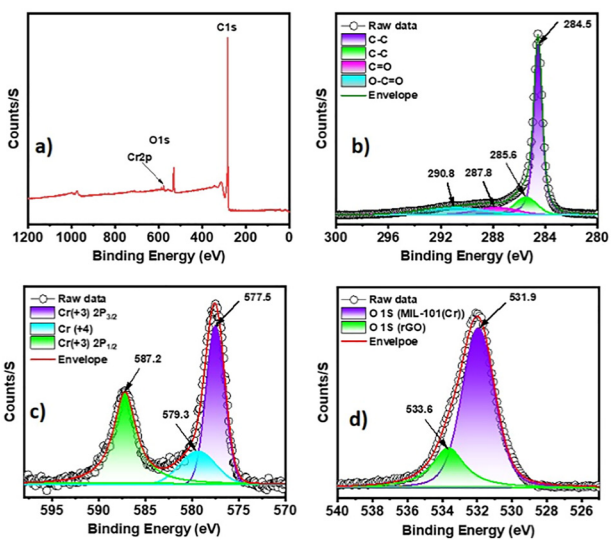

Fig. 8 XPS analysis of the rGO–20 wt% MIL-101(Cr) composite: (a) wide scan spectra and (b)–(d) high resolution C 1s, Cr 2p and O 1s spectra, respectively.

The observed energy difference of 9.7 eV between these peaks confirms the presence of Cr^{3+}. A smaller peak at 579.3 eV is attributed to Cr^{4+}. The O 1s spectrum (Fig. 8d) shows a peak at 531.9 eV, corresponding to oxygen in MIL-101(Cr). An additional smaller peak at 533.6 eV is assigned to O 1s from rGO.[36,37]

3.6. Sensitivity measurements

In the course of investigating the ammonia gas sensing properties of reduced graphene oxide (rGO) and its MIL-101(Cr) composites, the determination of the operating temperature was undertaken as a preliminary step. For this, 10 mg of rGO and 10 wt% MIL-101(Cr) composite were individually dispersed in 1 mL of ethanol *via* sonication for a duration of 5 min. Subsequently, a droplet of each dispersed solution was deposited onto the 3 mm active region of the ITD patterned PCB, followed by drying in a vacuum oven at a temperature of 100 °C for a period of 2 hours. The schematic of the experimental setup used for the gas sensing measurement is shown in Fig. S2. Upon cooling to ambient temperature, the PCB was employed to measure the resistance of the samples. The initial resistance measurements were conducted in an air environment (R_{air}) over a temperature range spanning from ambient to 150 °C, with the glass chamber maintained in an open state. Thereafter, 25 mL of ammonia gas was introduced into the sealed glass chamber, and resistance measurements were conducted in the same temperature range. The percentage sensitivity (%S) was calculated using the following formula:[39]

$$\%S = \frac{(R_{air} - R_{gas})}{R_{air}} \times 100$$

where R_{gas} represents the resistance in the presence of ammonia gas. A graphical representation of temperature *versus* percentage sensitivity for both rGO and the 10 wt% MIL-101(Cr) composite (Fig. 9) revealed that the operating temperature for ammonia gas detection is 115 °C.

Subsequently, a comprehensive investigation was conducted on MIL-101(Cr) composites with MIL-101(Cr) wt% ranging from 2.5 to 80, as well as pristine rGO. These materials were mounted on printed circuit boards (PCBs) following the aforementioned protocol. Upon reaching an operating temperature of 115 °C, the glass chamber was sealed, and resistance values were meticulously recorded at this temperature. Thereafter, a precise volume of 30 mL (6%, *i.e.* 60 000 ppm) of ammonia gas was injected into the chamber *via* a syringe. The chamber was maintained in a closed state for a duration of 10 min, allowing the measurement of resistance changes during the adsorption process, followed by a 10-min desorption period with the chamber open. This cyclic process, comprising 10 min of adsorption and 10 min of desorption, was repeated three times for 30 mL of ammonia gas. Analogous measurements were performed using varying volumes of gas, spanning from 25 mL to 1 mL (50 000 ppm to 2000 ppm). Following data acquisition, the percentage sensitivity (%S) was calculated for all composite variations and pristine rGO with respect to ammonia gas volumes ranging from 30 mL to 1 mL (Fig. 10a). Notably, the 20 wt% MIL-101(Cr) composite exhibited superior sensitivity across all ammonia gas volumes, with %S values of −18.87 for 30 mL and −16.58 for 25 mL of ammonia gas (Fig. 11). Furthermore, the 20 wt% MIL-101(Cr) composite exhibited remarkable detection sensitivity towards ammonia, with a

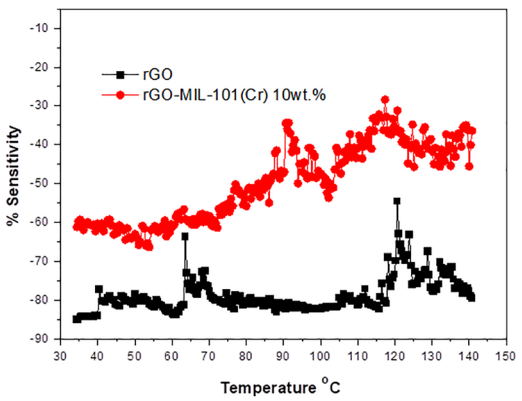

Fig. 9 Graph of %sensitivity *vs.* temperature for the determination of the operating temperature.

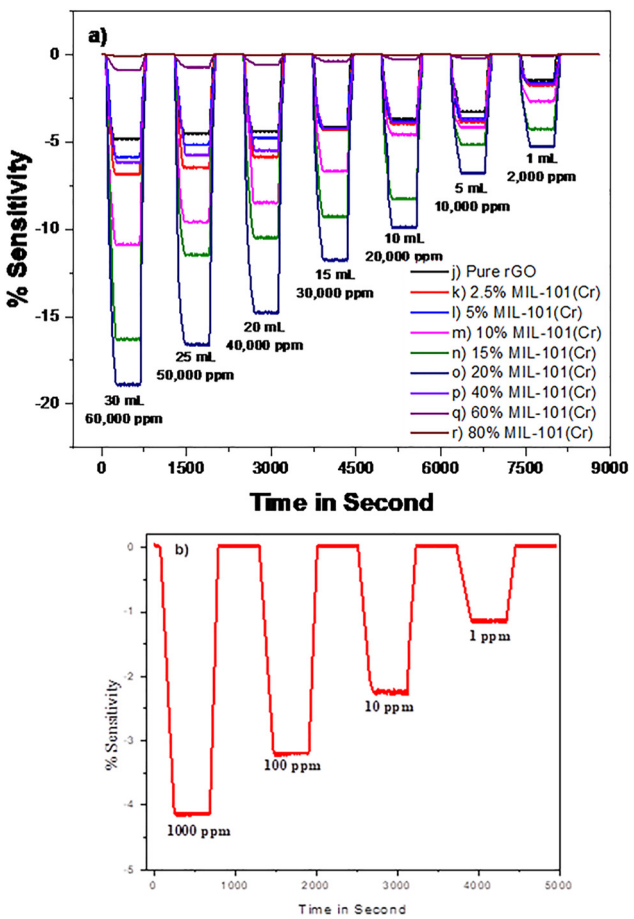

Fig. 10 (a) %Sensitivity for ammonia gas (60 000 ppm to 2000 ppm) using rGO and rGO–MIL-101(Cr) composites; (b) %sensitivity for ammonia (1000 ppm to 1 ppm) gas using the rGO–20 wt% MIL-101(Cr) composite.

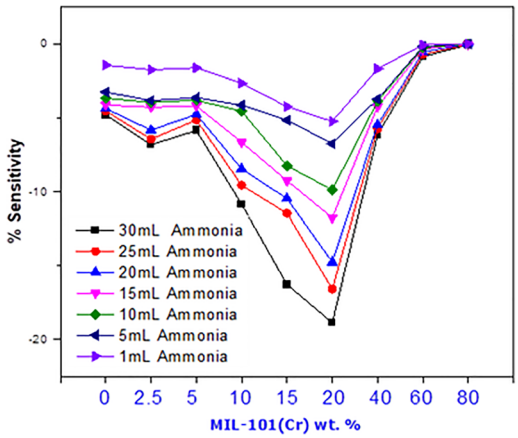

Fig. 11 Graph of %sensitivity *vs.* composite concentration with ammonia concentrations ranging from 30 mL (60 000 ppm) to 1 mL (2000 ppm).

detectable concentration as low as 1 ppm (Fig. 10b). Notably, the composite maintained its performance for ammonia gas detection even after one year, demonstrating stable and uniform detection levels across the tested concentration range (Fig. S3). This enduring performance underscores the exceptional stability and durability of the 20 wt% MIL-101(Cr) composite, rendering it a promising candidate for practical applications in ammonia sensing.

To evaluate the cross-sensitivity of the sensor, the 20 wt% MIL-101(Cr) composite was utilized, and similar measurements were conducted for 25 mL of various gases, including acetone, chloroform, toluene, benzene, methanol, and hydrogen. With the exception of acetone, all gases displayed a decrease in resistance subsequent to gas injection (Fig. 12). A comparative analysis of %*S* values for 25 mL of ammonia gas with those of the other gases (Fig. 12 and Table 3) revealed that ammonia gas exhibits significantly higher %*S* values, with most gases displaying positive sensitivities.

The rGO–MIL-101(Cr) composite exhibits p-type behavior upon exposure to oxidizing or reducing gases, attributed to the intrinsic p-type conductivity of rGO and the interaction of

Table 3 %Sensitivity for 5% of ammonia and other gases

S. No.	Gases	%Sensitivity
1	Ammonia	−16.58
2	Acetone	−1.37
3	Chloroform	1.3
4	Toluene	0.81
5	Benzene	2.79
6	Methanol	1.6
7	Hydrogen	1.36

gases with the MIL-101(Cr) component. When exposed to reducing gases, such as ammonia and acetone, these gases donate electrons to the p-type material, resulting in an increase in resistance, which leads to negative sensitivity values, as calculated by the %*S* formula. In contrast, oxidizing gases, including chloroform, toluene, benzene, methanol, and hydrogen, accept electrons, thereby increasing the hole concentration and reducing the electrical resistance of the p-type material, which manifests as positive sensitivity values, as determined by the %*S* formula.

This study evaluates the sensitivity of various gases at the operating temperature optimized for ammonia detection. A comparative analysis of the %*S* values for 25 mL of ammonia gas with those of the other gases (Fig. 12) revealed that ammonia gas exhibits a significantly higher %*S* value (−16.58) compared to the other gases (see Table 3). As anticipated, acetone exhibits a negative sensitivity value with a lower magnitude, whereas the other gases display positive sensitivity values. The sensitivity of each gas is highly dependent on the operating temperature and the composition of the MOF and rGO, which is why the other gases exhibit lower sensitivity values at the temperature optimized for ammonia detection.

The response and recovery times for the 20 wt% MIL-101(Cr) composite, when exposed to 25 mL of ammonia gas, were ascertained to be 105 seconds and 83 seconds, respectively (Fig. 13). Despite these values being marginally higher than those of a few other composites, the 20 wt% MIL-101(Cr) composite's superior sensitivity renders it a promising material

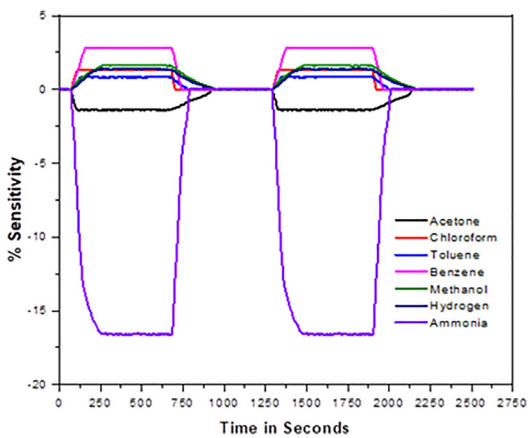

Fig. 12 %Sensitivity of various gases using the rGO–20 wt% MIL(Cr) composite.

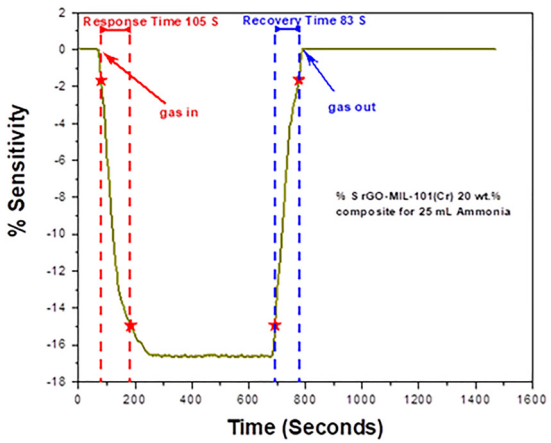

Fig. 13 Response and recovery times for ammonia gas using the rGO–20 wt% MIL-101(Cr) composite.

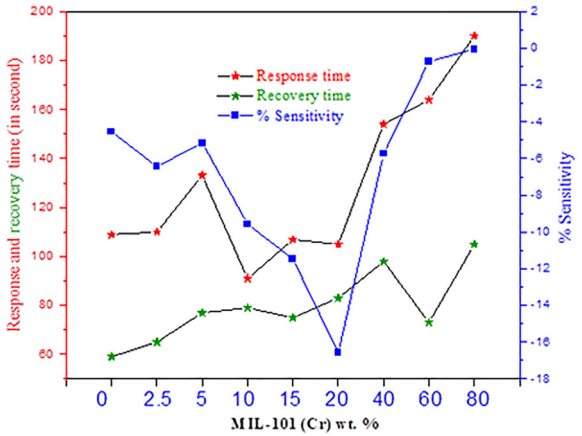

Fig. 14 Response and recovery times and %sensitivity for ammonia gas using rGO and rGO–MIL-101(Cr) composites.

for applications involving ammonia gas sensing, as evidenced by its performance characteristics (Fig. 14).

A comprehensive comparison of our results with previously reported ammonia sensors is presented, considering key performance indicators such as the detection range, detection limit, response time, recovery time, sensitivity, selectivity, stability, reproducibility, and operating temperature (OT). The details are summarized in Table S1 (SI), which encompasses a diverse range of gas sensors based on conventional solid-state materials, including semiconducting metal oxides and organic polymers, as well as unconventional materials like carbon nanotubes (CNTs), graphene, and metal–organic frameworks (MOFs). These sensors have been evaluated using various working methodologies, fabrication techniques, and device integration approaches. While some of these sensors exhibit promising performance, they often compromise on one or two critical performance indicators. In contrast, our material demonstrates high sensitivity, excellent response and recovery times, notable selectivity towards interfering gases, and consistent performance even after one year, down to 1 ppm. Given the emphasis on practical applications and real-world performance, many of these sensors may suffer from instability in moist environments, which can significantly limit their practical utility. In contrast, the MIL-101(Cr) component in our composite exhibits a high surface area and remarkable stability under moist conditions, rendering it an attractive option for real-world applications.

3.7. Sensing mechanism

As previously described, we synthesized rGO–MIL-101(Cr) composites with varying MIL-101(Cr) percentages, which we subsequently evaluated for their ammonia gas sensing capabilities. Notably, the rGO–MIL-101(Cr) composite represents a novel material, and this study represents the first report on its application in ammonia gas detection. We found that the operating temperature for this ammonia gas sensing is 115 °C. Herein, we have optimized the composition of rGO and MIL-101(Cr) and found that, among the synthesized compositions, the 20 wt% rGO–MIL-101(Cr) variant demonstrated the highest selective sensing response towards ammonia gas in the presence of other gases like acetone, chloroform, toluene, benzene, methanol and hydrogen with %S of −18.87 for 30 mL (60 000 ppm) ammonia gas and −16.58 for 25 mL (50 000 ppm) ammonia gas.

The inherent non-conductivity of MIL-101(Cr) arises from its electronic structure, which features metal–ligand interactions and aromatic linkers that impede the free flow of electrons necessary for electrical conductivity. Conversely, rGO exhibits conductivity due to its sp^2 hybridized carbon structure, facilitating electron mobility along the conjugated network and manifesting p-type behavior attributed to oxygen-containing functional groups and defects.[40] This dichotomy in conductivity influences the composite's behavior, with rGO dominating the electrical properties and MIL-101(Cr) modulating them *via* ammonia gas adsorption. The sensing mechanism entails the interaction between ammonia molecules and the p-type MIL-101(Cr) framework, resulting in electron donation, reduced hole concentration, and increased resistance, thereby inducing a change in electrical conductivity. Experimental evidence corroborates this p-type behavior and negative sensitivity of the composite, rather than just being assumed due to the presence of rGO. Compositional optimization revealed that 20% MIL-101(Cr) yields enhanced sensor performance, culminating in the highest ammonia gas sensing response.

Pristine rGO, a p-type material, possesses an excess of holes (positive charge carriers) due to its inherent electronic structure (Fig. 15a). However, its limited surface area results in minimal ammonia molecule adsorption, leading to a reduced number of

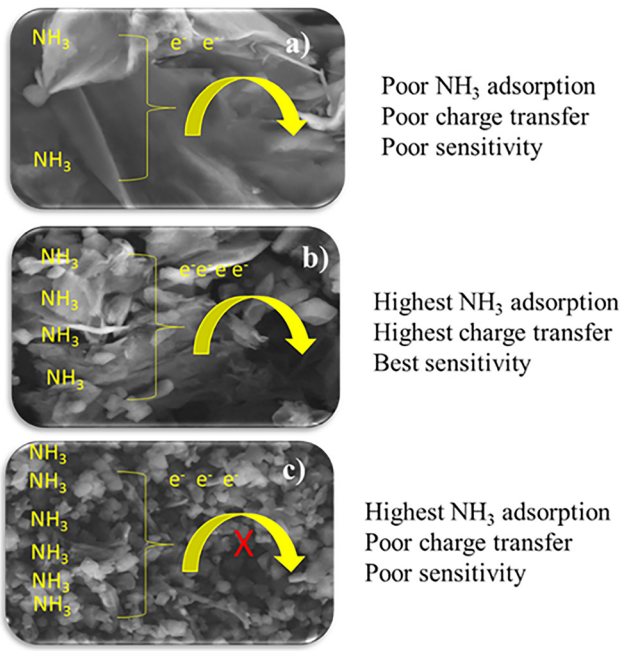

Fig. 15 NH_3 sensing mechanism using (a) the rGO–2.5 wt% MIL-101(Cr) composite, (b) the rGO–20 wt% MIL-101(Cr) composite and (c) the rGO–80 wt% MIL-101(Cr) composite.

electrons available for charge transfer and consequently a lower sensitivity. Below 20% MIL-101(Cr) loading, the limited surface area results in fewer ammonia molecules being adsorbed, leading to reduced charge transfer and sensitivity. As the MIL-101(Cr) content increases up to 20% (as can be seen from FESEM and TEM images), the sufficient quantity of rGO and increased adsorption of ammonia molecules enable more electrons to be donated to rGO, filling more holes and facilitating charge transfer, thereby enhancing the sensing response (Fig. 15b).

With increasing MIL-101(Cr) content, the ammonia adsorption capacity increases, leading to enhanced charge transfer and sensitivity. However, beyond a certain threshold, the excessive MIL-101(Cr) loading disrupts the percolation network of rGO, reducing conductivity and charge transfer efficiency. Our experimental results indicate that 20 wt% MIL-101(Cr) loading achieves the optimal balance between these two competing factors, where the benefits of increased ammonia adsorption are maximized without compromising the conductive pathways. This balance is likely due to the fact that as the MIL-101(Cr) content increases, the distance between rGO sheets also increases, eventually disrupting the conductive pathways and reducing the charge transfer efficiency. At 20 wt% MIL-101(Cr) loading, the morphology of the composite, as seen from FESEM and TEM images, suggests an optimal distribution of MIL-101(Cr) and rGO, enabling efficient charge transfer and maximizing sensitivity.

Above 20% MIL-101(Cr) loading, as the MIL-101(Cr) content increases, the BET surface area expands, providing additional adsorption sites. However, beyond the optimal 20% loading, the insulating nature of MIL-101(Cr) compromises the composite's electrical conductivity, dominating the sensing response and diminishing sensitivity. Excessive MIL-101(Cr) loading disrupts this percolation network (Fig. 15c), reducing conductivity and charge transfer efficiency, *i.e.* the distance between rGO sheets increases due to excessive MIL-101(Cr) loading (as observed for FESEM 80% MIL-101(Cr)). The percolation threshold is the critical concentration of MIL-101(Cr) at which the network of conductive pathways of rGO becomes continuous, facilitating efficient charge transfer.

A synergistic effect is evident between rGO and MIL-101(Cr), wherein MIL-101(Cr) provides active sites for gas sensing and a large surface area, while rGO enhances conductivity and charge transfer. This synergy confers unique properties, including selective sensitivity in the presence of other gases. The Gaussian trend in sensitivity can be attributed to the interplay between gas adsorption capacity and electrical conductivity. The optimal balance between these two factors is achieved at 20% MIL-101(Cr) loading, resulting in the highest sensitivity.

4. Conclusion

This pioneering study demonstrates the transformative potential of rGO–MIL-101(Cr) composites for selective ammonia gas sensing, unlocking new avenues for environmental monitoring, industrial safety, and healthcare applications. By optimizing the composition of rGO and MIL-101(Cr), we identified the 20 wt% variant as the most effective, exhibiting a high sensitivity towards ammonia gas [−18.87 for 60 000 ppm (6%) and −5.24% for 2000 ppm (0.2%)] while maintaining selectivity in the presence of other gases. This composite demonstrates exceptional potential for ammonia detection, retaining its remarkable sensitivity down to 1 ppm even after one year, thereby underscoring its stability and durability for practical sensing applications. The synergistic effect between rGO's conductivity and MIL-101(Cr)'s high surface area and gas adsorption capacity enables enhanced sensing performance. Our findings provide valuable insights into the design and development of novel MOF-based composites for advanced gas sensing applications. Notably, this study constitutes a significant step forward in the field, offering a new paradigm for gas sensing technologies. As we look to the future, our findings pave the way for scalable synthesis methods, real-world deployment, and further innovation in gas sensing technologies. Future research directions could involve exploring the applicability of these composites in real-world settings, investigating their stability and durability, and developing scalable synthesis methods. Ultimately, this work contributes to a safer, more sustainable world by enabling the detection of hazardous gases and promoting environmental stewardship.

Author contributions

SCM performed the experimental work, characterized and analyzed the data and prepared the original draft of the manuscript. GGU helped in gas sensing measurements. AGK revised the manuscript and contributed to the interpretation of results. BBK revised the manuscript. SSA conceived the concept and methodology, analyzed the data, supervised the work, and validated and reviewed the manuscript.

Conflicts of interest

There are no conflicts to declare.

Data availability

The authors confirm that the data supporting the findings of this study are available within the article. Raw data that support the findings of this study are available from the corresponding author upon reasonable request.

The data supporting this article have been included as part of the supplementary information (SI). Supplementary information: XRD analysis of MIL-101(Cr), schematic of the gas measurement setup, ammonia sensing performance of the rGO–20 wt% MIL-101(Cr) composite down to 1 ppm after one year, and comparison of the performance of ammonia gas sensors. See DOI: https://doi.org/10.1039/d5ma01104c.

Acknowledgements

SCM is grateful to the Director, C-MET Pune for providing characterization support.

References

1 M. P. Suh, H. J. Park, T. K. Prasad and D.-W. Lim, *Chem. Rev.*, 2012, **112**, 782–835.
2 M. O'Keeffe and O. M. Yaghi, *Chem. Rev.*, 2012, **112**, 675–702.
3 S. Xin, Y. Wang, Z. Wang, R. Li, J. Yan and Y. Chen, *Phys. Lett. A*, 2025, **535**, 130277.
4 A. H. Assen, O. Yassine, O. Shekhah, M. Eddaoudi and K. N. Salama, *ACS Sens.*, 2017, **2**, 1294–1301.
5 D. Kwak, Y. Lei and R. Maric, *Talanta*, 2019, **204**, 713–730.
6 H. Wang, S. Nie, H. Li, R. Ali, J. Fu, H. Xiong, J. Li, Z. Wu, W.-M. Lau, N. Mahmood, R. Jia, Y. Liu and X. Jian, *ACS Sens.*, 2019, **4**, 2343–2350.
7 H. Spieser, Z. Tehrani, M. M. Ali, E. D. Ahmadi, A. Denneulin, J. Bras, D. Deganello and D. Gethin, *J. Mater. Chem. C*, 2021, **9**, 6332–6343.
8 S. Ali, M. A. Jameel, G. Oldham, A. Gupta, M. Shafiei and S. J. Langford, *J. Mater. Chem. C*, 2022, **10**, 1326–1333.
9 L. S. SP, M. Rajkumar, K. Govindharaj, J. Mobika and R. K. Thangavelu, *J. Mater. Chem. C*, 2023, **11**, 16333–16345.
10 R. J. Rath, W. B. Zhang, O. Kavehei, F. Dehghani, S. Naficy, S. Farajikhah and F. Oveissi, *ACS Sens.*, 2024, **9**, 2836–2845.
11 C. N. G. Weir, R. J. Blanchard, A. P. Parsons, G. Kalarikkandy and M. J. Katz, *J. Mater. Chem. C*, 2024, **12**, 125–131.
12 L. Gong, S. Jin, R. Liu, Z. Liu, Y. Zhang, L. Zhang, T. Zhao, H. Fa and W. Yin, *Microchem. J.*, 2024, **205**, 111262.
13 A. Verma and T. Kumar, *Mater. Adv.*, 2024, **5**, 7387–7400.
14 A. Kashyap, B. Chakraborty, T. Hazarika, S. Chouhan, B. Kakati and H. Kalita, *Mater. Adv.*, 2025, **6**, 3828–3840.
15 A. Thomas and K. Sivaperuman, *Mater. Adv.*, 2025, **6**, 629–640.
16 A. Verma, T. Kumar and R. Singhal, *Mater. Adv.*, 2025, **6**, 1869–1882.
17 C. Bae, G. Jeong, S. Park, Y. Kim, M. Gu, D. Kim and J. Kim, *ACS Omega*, 2022, **7**, 17144–17150.
18 E. Haghighi and S. Zeinali, *RSC Adv.*, 2019, **9**, 24460–24470.
19 Y. Benseghir, M. Y. Tsang, F. Schöfbeck, D. Hetey, T. Kitao, T. Uemura, H. Shiozawa, M. R. Reithofer and J. M. Chin, *J. Colloid Interface Sci.*, 2025, **678**, 979–986.
20 Y.-K. Seo, J. W. Yoon, J. S. Lee, Y. K. Hwang, C.-H. Jun, J.-S. Chang, S. Wuttke, P. Bazin, A. Vimont, M. Daturi, S. Bourrelly, P. L. Llewellyn, P. Horcajada, C. Serre and G. Férey, *Adv. Mater.*, 2012, **24**, 806–810.
21 A. Ahmed, A. Singh, S.-J. Young, V. Gupta, M. Singh and S. Arya, *Composites, Part A*, 2023, **165**, 107373.
22 G. Férey, C. Mellot-Draznieks, C. Serre, F. Millange, J. Dutour, S. Surblé and I. Margiolaki, *Science*, 2005, **309**, 2040–2042.
23 K. Leng, Y. Sun, X. Li, S. Sun and W. Xu, *Cryst. Growth Des.*, 2016, **16**, 1168–1171.
24 S. Kayal, B. Sun and A. Chakraborty, *Energy*, 2015, **91**, 772–781.
25 H.-H. Huang, K. K. H. De Silva, G. R. A. Kumara and M. Yoshimura, *Sci. Rep.*, 2018, **8**, 6849.
26 N. Yusoff, P. Rameshkumar, M. M. Shahid, S.-T. Huang and N. M. Huang, *Microchim. Acta*, 2017, **184**, 3291–3299.
27 T. F. Emiru and D. W. Ayele, *Egypt. J. Basic Appl. Sci.*, 2017, **4**, 74–79.
28 D. Vasudevan, D. Senthilkumar and S. Surendhiran, *Int. J. Thermophys.*, 2020, **41**, 74.
29 M. Anbia and V. Hoseini, *Chem. Eng. J.*, 2012, **191**, 326–330.
30 M. Shafiei, M. S. Alivand, A. Rashidi, A. Samimi and D. Mohebbi-Kalhori, *Chem. Eng. J.*, 2018, **341**, 164–174.
31 K. C. Chong, P. S. Ho, S. O. Lai, S. S. Lee, W. J. Lau, S.-Y. Lu and B. S. Ooi, *Sustainability*, 2022, **14**(3), 1152.
32 T. Loiseau and G. Férey, *J. Fluor. Chem.*, 2007, **128**, 413–422.
33 C. Serre, J. A. Groves, P. Lightfoot, A. M. Z. Slawin, P. A. Wright, N. Stock, T. Bein, M. Haouas, F. Taulelle and G. Férey, *Chem. Mater.*, 2006, **18**, 1451–1457.
34 P. M. Förster, A. R. Burbank, C. Livage, G. Férey and A. K. Cheetham, *Chem. Commun.*, 2004, 368–369, DOI: 10.1039/B311156C.
35 P. M. Förster, N. Stock and A. K. Cheetham, *Angew. Chem., Int. Ed.*, 2005, **44**, 7608–7611.
36 B. E. Keshta, H. Yu, L. Wang, H. Yi, S. Jian, M. D. A. Uddin, C. Ouyang, Y. Wang, X. Yuan, Y. Zhang, Y. Jin, A. Basit, M. Owais Malik and K. M. Awan, *npj Clean Water*, 2025, **8**, 15.
37 J. Gu, X. Yin, X. Bo and L. Guo, *ChemElectroChem*, 2018, **5**, 2893–2901.
38 S. Tamang, S. Rai, R. Bhujel, N. K. Bhattacharyya, B. P. Swain and J. Biswas, *J. Alloys Compd.*, 2023, **947**, 169588.
39 W. Zang, W. Wang, D. Zhu, L. Xing and X. Xue, *RSC Adv.*, 2014, **4**, 56211–56215.
40 D.-T. Phan and G.-S. Chung, *J. Phys. Chem. Solids*, 2013, **74**, 1509–1514.